



Original Contribution

Molecular Identity Changes of Tumor-Associated Macrophages and Microglia After Magnetic Resonance Imaging–Guided Focused Ultrasound–Induced Blood–Brain Barrier Opening in a Mouse Glioblastoma Model

Yanrong Zhang^a, Jing Wang^{a,b}, Sara Natasha Ghobadi^a, Haiyan Zhou^{a,c}, Ai Huang^{a,d}, Marco Gerosa^{a,e}, Qingyi Hou^{a,f}, Olivier Keunen^g, Anna Golebiewska^h, Frezghi G. Habteⁱ, Gerald A. Grant^j, Ramasamy Paulmurugan^k, Kevin S. Lee^l, Max Wintermark^{m,*}

^a Department of Radiology, Neuroradiology Division, Stanford University, Stanford, CA, USA

^b Department of Radiology, Shandong Provincial Hospital Affiliated to Shandong First Medical University, Jinan, China

^c Acupuncture and Tuina School/Third Teaching Hospital, Chengdu University of Traditional Chinese Medicine, Chengdu, Sichuan, China

^d Cancer Center, Union Hospital, Tongji Medical College, Huazhong University of Science and Technology, Wuhan, China

^e Department of Diagnostic and Public Health, University of Verona, Verona, Italy

^f Department of Nuclear Medicine, Guangdong Provincial People's Hospital, Guangzhou, China

^g In Vivo Imaging Facility, Luxembourg Institute of Health, Luxembourg

^h Department of Oncology, Luxembourg Institute of Health, Luxembourg

ⁱ Department of Radiology, Molecular Imaging Program at Stanford, Stanford, CA, USA

^j Division of Pediatric Neurosurgery, Department of Neurosurgery, Lucile Packard Children's Hospital, Stanford University School of Medicine, Stanford, CA, USA

^k Molecular Imaging Program at Stanford (MIPS), Canary Center for Cancer Early Detection, Department of Radiology, Stanford University, Stanford, CA, USA

^l Departments of Neuroscience and Neurosurgery and Center for Brain, Immunology, and Glia, School of Medicine, University of Virginia, Charlottesville, VA, USA

^m Department of Neuroradiology, University of Texas MD Anderson Cancer Center, Houston, TX, USA

ARTICLE INFO

Keywords:

Sterile inflammation

Glioblastoma

Tumor-associated macrophages and microglia

Microglia and macrophage activation

Focused ultrasound

Magnetic resonance imaging–guided focused ultrasound

Microbubbles

An orthotopically allografted mouse GL26 glioma model (Ccr2^{RFP/wt}–Cx3cr1^{GFP/wt}) was used to evaluate the effect of transient, focal opening of the blood–brain barrier (BBB) on the composition of tumor-associated macrophages and microglia (TAMs). BBB opening was induced by magnetic resonance imaging (MRI)–guided focused ultrasound (MRgFUS) combined with microbubbles. CX3CR1-GFP cells and CCR2-RFP cells in brain tumors were quantified in microscopic images. Tumors in animals treated with a single session of MRgFUS did not exhibit significant changes in cell numbers when compared with tumors in animals not receiving FUS. However, tumors that received two or three sessions of MRgFUS had significantly increased amounts of both CX3CR1-GFP and CCR2-RFP cells. The effect of MRgFUS on immune cell composition was also characterized and quantified using flow cytometry. Glioma implantation resulted in increased amounts of lymphocytes, monocytes and neutrophils in the brain parenchyma. Tumors administered MRgFUS exhibited increased numbers of monocytes and monocyte-derived TAMs. In addition, MRgFUS-treated tumors exhibited more CD80+ cells in monocytes and microglia. In summary, transient, focal opening of the BBB using MRgFUS combined with microbubbles can activate the homing and differentiation of monocytes and induce a shift toward a more pro-inflammatory status of the immune environment in glioblastoma.

Introduction

Glioblastoma (GBM) is the most common and most lethal primary malignancy of the central nervous system. With an incidence of 2–3 per 100,000 population, GBM constitutes up to 54% of all gliomas and 16% of all primary brain tumors [1]. Even with multimodal treatments including surgery, chemotherapy and radiotherapy, the median survival time for patients with GBM is only 14.6 mo [2,3]. Despite recent advances in the development of novel therapies against extracranial tumors,

very little progress has been made in terms of patient outcome for the treatment of GBM [4]. The lack of progress in the development of novel therapies for brain tumors can be attributed, at least in part, to the difficulty involved in therapeutic agents crossing the blood–brain barrier (BBB) and the dose limited-toxicity that restricts the injection of therapeutic dosages.

The BBB regulates access to the the central nervous system through a tightly regulated neurovascular unit (NVU) including endothelial cells (ECs), pericytes and astrocytic endfeet, which together control the

* Corresponding author. Department of Neuroradiology, University of Texas MD Anderson Cancer Center, 1400 Pressler Street, Unit 1482, Houston, TX 77030-4009, USA.

E-mail address: Max.Wintermark@gmail.com (M. Wintermark).

<https://doi.org/10.1016/j.ultrasmedbio.2022.12.006>

Received 31 August 2022; Revised 11 November 2022; Accepted 10 December 2022

passage of nutrients and metabolites from the bloodstream to the brain parenchyma. However, these same features also hinder the delivery of systemic therapies into brain tumors. Although the BBB is often disrupted in brain tumor tissue, the disruption is heterogeneous and allows only smaller molecules to enter, resulting in inadequate drug accumulation in glioblastomas [5,6]. Consequently, the structural and functional heterogeneity of the BBB in the brain tumor microenvironment needs to be considered when attempting to develop effective, systemically delivered therapies. Multiple strategies are being developed to regulate or disrupt the BBB, including the use of osmotic agents [7–9] and the design of molecules using receptor-mediated transport [10].

The combination of transcranial magnetic resonance imaging (MRI)–guided focused ultrasound (MRgFUS) with intravenous microbubbles has also emerged as an effective strategy for non-invasively opening the BBB [11]. MRgFUS oscillates microbubbles and mechanically disrupts the BBB in a targeted, transient and non-invasive manner, increasing the vascular permeability of the brain to large molecules [12–14]. In pre-clinical studies, MRgFUS-induced opening of the BBB has been used to deliver chemotherapeutic agents [15,16], antibodies [17,18], stem cells [19] and therapeutic genes [20]. Extensive pre-clinical research has indicated that FUS with microbubbles can lead to a more than fourfold increase in the delivery and penetration of a range of intravenously administered anti-cancer agents in brain tumors [21]. This improvement in the delivery of anti-cancer agents has also led to a significant increase in the median survival time (threefold) in multiple orthotopic murine tumor models, including glioma and breast cancer brain metastases [22].

Most of the research on MRgFUS-induced BBB opening has focused on using this approach to increase the concentration of therapeutic agents in brain tumors. However, MRgFUS by itself may also directly induce some immune-related responses. Studies on naïve animals have revealed that MRgFUS-induced BBB opening elicits sterile inflammation in the normal brain microenvironment. MRgFUS-induced opening of the BBB triggers an acute increase in the transcription of pro-inflammatory cytokines [23,24]. In intracranial tumor models, MRgFUS combined with microbubbles has also had immunomodulatory effects [25]. MRgFUS-treated gliomas exhibit an increase in the CD8⁺/T-reg ratio, a metric commonly correlated with improved treatment outcome [26]. The immunomodulatory influence of MRgFUS combined with microbubbles on the BBB may thus provide an opportunity for synergy of MRgFUS and immune-based therapeutics that could generate a stronger clinical response. A key step in evaluating this intriguing possibility is investigating how MRgFUS affects the tumor-associated macrophages and microglia (TAMs) in the GBM–TAM pool.

In the current study, we applied MRgFUS together with microbubbles to an immunocompetent mouse glioma model based on orthotopic implantation of GL26 glioma cells. To investigate the composition and functional status of myeloid populations after BBB opening, tumor cells were allografted to *Ccr2^{RFP/wt}Cx3cr1^{GFP/wt}* mice carrying genetically color-coded microglia (*Cx3cr1-GFP*) and blood-derived monocytes and macrophages (*Ccr2-RFP*). Multistain immunocytochemistry and flow cytometry (FCM) were used to define the changes in TAMs after MRgFUS treatment.

Methods

Study design

The animal protocol for this study was approved by the Stanford University Administrative Panel on Laboratory Animal Care (APLAC). All experiments were conducted in accordance with the National Institutes of Health's *Guide for the Care and Use of Laboratory Animals*. Two series of experiments were carried out, one for histological analysis and one for FCM analysis.

Thirty mice with brain tumors were divided into six groups that received the following treatments prior to histology analysis:

- Group 1: No-MRgFUS control group animals were euthanized when the tumors were 4–5 mm in diameter (n = 5).
- Group 2: MRgFUSx1 animals underwent one session of MRgFUS when the tumors were 4 mm in diameter and were euthanized 2 d after MRgFUS (n = 5).
- Group 3: MRgFUSx2 animals underwent two sessions of MRgFUS every other day, starting when the tumors were 3–4 mm in diameter, and were euthanized 2 d after the second session (n = 5).
- Group 4: MRgFUSx3—animals underwent three sessions of MRgFUS, once every other day, starting when the tumors were a 2–3 mm in diameter, and were euthanized 2 d after the last session (n = 5).

The other 10 animals were divided into two groups that received the following treatments prior to FCM analysis.

- Group 5: Tumor_No FUS animals were euthanized when the tumors were 4–5 mm in diameter (n = 5).
- Group 6: Tumor_FUS animals underwent three sessions of MRgFUS, once every other day, starting when the tumors were a 2–3mm in diameter, and were euthanized 2 d after the last session (n = 5).

Three naïve animals without brain tumors were euthanized to collect brain tissue for FCM analysis.

Cell line and culture

The GL26 mouse glioma cell line was provided by Dr. Ramasamy Paulmurugan and maintained in medium consisting of Dulbecco's modified Eagle's medium (DMEM), 10% fetal bovine serum (FBS), 100 μ L/mL penicillin–streptomycin and 4 mM L-glutamine.

Mice

All mice were housed under specific pathogen-free conditions at a barrier facility at the Canary Center at Stanford University School of Medicine (Stanford, CA, USA). All animal handling, surveillance and experimentation was performed in accordance with and approval from the Stanford University Administrative Panel on Laboratory Animal Care.

Homozygous *Ccr2^{RFP/RFP}* mice (JAX Stock No. 017586) [27] and *Cx3cr1-GFP* mice (JAX Stock No. 005582) [28] on a C57BL/6 background were purchased from the Jackson Laboratory (Bar Harbor, ME, USA) and intercrossed to yield *Ccr2^{RFP/wt}Cx3cr1^{GFP/wt}* animals. To confirm the establishment of heterozygous mice, ear snips were collected when the offspring were 15 through 18 d old, and genotyping was performed using a commercial assay service (Transnetx, Inc., Cordova, TN, USA). Previous studies [29] had indicated that implantation of murine GL261 glioma cells into *Ccr2^{RFP/wt}Cx3cr1^{GFP/wt}* mice allowed for efficient evaluation of the myeloid cells, known to constitute the majority of CD45⁺ immune cells in gliomas. Immunohistochemistry allows for discrimination of CX3CR1-GFP⁺ microglia and TAMs derived thereof and CCR2-RFP⁺ blood-derived monocytes and monocyte-derived TAMs within the tumor as well as in surrounding adjacent brain.

Orthotopic syngeneic model of mouse brain tumors

Mouse glioma GL26 cells dissociated into single-cell suspensions were orthotopically injected into the brains of 8- to 10-wk-old *Ccr2^{RFP/wt}Cx3cr1^{GFP/wt}* mice using stereotactic injection. In brief, mice were anesthetized with 3% isoflurane (Minrad International, Buffalo, NY, USA) in an induction chamber. Anesthesia on the stereotactic frame (David Kopf Instruments, Tujunga, CA, USA) was maintained with 2% isoflurane/L oxygen delivered through a nose adaptor. A burr hole was placed 1.7 mm lateral and 2 mm posterior of bregma. A blunt-ended needle (75 N, 26s gauge, 2 in, point style 2, 5 μ L; Hamilton Co., Reno, NV, USA)

was lowered into the burr hole to a depth of 3.5 mm below the dura surface and retracted 0.5 mm to form a small reservoir. A microinjection pump (UMP-3; World Precision Instruments, Sarasota, FL, USA) was used to inject 4×10^5 GL26 cells in a volume of 3 μL at 30 nL/s. After being left in place for 1 min, the needle was retracted at 3 mm/min. The cranial injection site was sealed using biodegradable glue. Tumor formation was followed by MRI using a 3-T scanner from MR Solutions. From 1 wk post-tumor implantation, T2 fast spin echo (FSE, repetition time/echo time [TR/TE] = 4800/68 ms, flip angle = 90° , two averages, field of view [FOV] = 28 mm, matrix size = 256×248 , slice thickness = 1.0 mm) images were acquired once every 2 d to monitor the growth of the tumor. T2*-weighted gradient echo images (TR/TE = 391/13 ms, flip angle = 20° , three averages, FOV = 28 mm, matrix size = 256×256 , slice thickness = 1.0 mm) were obtained to identify possible hemorrhage.

MRgFUS setup and treatment protocol

Magnetic resonance imaging-guided focused ultrasound was delivered to open the BBB. The MRgFUS system (Image Guided Therapy, Pessac, France) was configured as described in previous studies [30,31]. The system included an MR-compatible, pre-focused, eight-element annular array, 1.5-MHz transducer (spherical radius = 20 ± 2 mm, active diameter = 25 mm [focal ratio = 0.8]; Imasonic, Voray sur l'Oignon, France), which was connected to a phased array generator and radiofrequency power amplifier. The transducer and animals were prepared as described in a previous study [32]. The membrane in front of the transducer was filled with de-gassed water and acoustic gel was applied between the transducer and skin. For sonication, the animals were placed in a prone position and maintained in that position using a bite bar and ear bars. The scalp hair was shaved and removed with depilatory cream. The experimental apparatus in this study is illustrated in Figure 1.

Definity Microbubbles (mean diameter range = 1.1–3.3 μm , mean concentration = 1.2×10^{10} bubbles/mL, diluted by 1:20 using $1 \times$ phosphate-buffered saline [PBS] = 300 $\mu\text{L}/\text{kg}$, Lantheus Medical Imaging, North Billerica, MA, USA) were injected through a catheter placed in the tail vein just before sonication (1.5 MHz, pulse duration = 20 ms, duty cycle = 2%, 1-Hz pulse repetition frequency, 90-s duration per sonication). Multiple sonications were administered in the vicinity of the targeted area of the brain by moving the sonication zones slightly rostrocaudally and medio-laterally targeting the brain tumors. An MR-compatible motorized positioning stage was used to move the transducer in the rostral-caudal and medial-lateral directions. After determination of the coordinates of the focal point within the MRI space, treatment planning MRI was acquired, and the focal region was positioned within the tumor. Ultrasound bursts were then applied at peak negative pressure of 0.5 MPa.

MRI data collection

On the day prior to and the day immediately after MRgFUS, a set of MRI data including T2-FSE, T2*-weighted gradient echo, dynamic contrast-enhanced (DCE) and post-contrast T1-weighted images were obtained.

The pre- and post-MRgFUS T2-FSE images were acquired to assess the size and location of the resulting lesions, T2*-weighted gradient echo images were obtained to identify possible hemorrhagic complications from the MRgFUS procedure. To obtain quantitative measurements of BBB permeability, a bolus of gadodiamide contrast (gadobenate dimeglumine, Multihance, Bracco Diagnostics Inc., Monroe Township, NJ, USA) was injected intravenously for DCE imaging (TR/TE = 34/3 ms, average = 1, FOV = 28 mm², flip angle = 20°). Post-contrast T1-weighted imaging (TR/TE = 620/12 ms, 2 averages, FOV = 28 mm, matrix size = 256×244 , slice thickness = 1 mm) was used to confirm the opening of the BBB after DCE imaging. Images were reviewed and analyzed using the Horos DICOM viewer. With the U.S. Food and Drug Administration-approved commercial software NordicICE (Nordic Neuro Lab, Bergen, Norway), Ktrans maps were computed using a pipeline inspired by that of Anzalone et al. [33]. Notably, local arterial input function (AIF) adapted for mice studies was extracted from the signal curves using a blind deconvolution method [34].

Tissue preparation and analysis

Mice were euthanized by inhalation of 3% isoflurane 2 d after the last MRgFUS session that perfused through the left ventricle at 15 mL/min for 1 min with 0.9% NaCl and then for 30 min with 4% paraformaldehyde in 0.1 M PBS (pH 7.4). Brains tissues were post-fixed overnight at 4°C and then transferred into 30% (w/v) sucrose in PBS. After equilibrating in the 30% sucrose solution, the brains were sectioned coronally (30 μm) with a sliding microtome. Sections were collected in 30% ethylene glycol and 25% glycerol in 50 mM PBS and stored at -20°C until used. A 1-in-6 series of sections were collected for nuclear counterstaining with Invitrogen Hoechst 33342 dye. Coronal brain sections containing tumors were acquired with a NanoZoomer Digital Pathology slide scanning system (Hamamatsu Photonics, K.K., Hamamatsu, Shizuoka, Japan).

To analyze the histological images, a custom analysis pipeline was set up to provide a tool able to quantify in a semi-automated manner the number of GFP- and RFP-labeled cells per square millimeter on the brain sections. On the images of the stained sections of the brain through NanoZoomer, a region of interest (ROI) was drawn around the brain tumor with the Freehand drawing tool of NDP.view2 software (Hamamatsu Photonics, K.K., Japan) by investigators blinded to the identity of the animals and sections they were analyzing. To minimize the bias in quantifying the GFP- and RFP-labeled cells, the red and green channels



Figure 1. Experimental apparatus and post-contrast T1-weighted image immediately after sonication. (A) Magnetic resonance imaging-guided focused ultrasound system consisting of a 1.5-MHz transducer (T) that rests on the top of the mouse head, can move in x–y planes and can be focused in the z-axis. (B) A 3-T magnetic resonance imaging scanner was used to detect blood–brain barrier opening after sonication. (C) Post-contrast T1-weighted image acquired immediately after sonication. Enhancement of the tumor (white arrow) and the brain tissue along the acoustic beam below the tumor (black arrow) indicates the area of blood–brain barrier opening.

were both set both at full dynamic ranges of 200% while the dynamic range of the blue channel was switched to 0% and turned off. A simple filter was used to improve the resolution of the image, and a magnification factor of 1.8% to 2.5% was applied to the ROIs. Then, the images were exported in .jpg files and analyzed in FIJI (ImageJ). FIJI is an open-source software commonly used for biomedical image analysis [35]. On loading the images in FIJI, the background was first removed using the Rolling Ball Radius algorithm [36,37]. The red and green channels were then split, and considering the different sizes of the RFP- and GFP-labeled cells, two different radii were adopted to subtract the red and the green components from the background. Otsu thresholding was used on the red and green channel images separately to distinguish positive from negative signals [38]. The group above the threshold (automatically computed based on signal intensity on the gray scale) was recognized as the effective signal from the labeled cells, and the group below the threshold was recognized as background noise and discarded. The application of a binary mask was followed by the watershed separation as a robust segmentation method, based on the average size of recognized single cells [39]. Finally, a simple particle counting method was applied to the resulting images (for the green and red channels) taking into account the average size of the single cells to quantify the numbers of GFP and RFP cells per square millimeter. A *t*-test was used to compare the numbers of GFP and RFP cells per square millimeter from two different groups.

FCM analysis

Mice were deeply anesthetized with 1%–4% isoflurane through a nosecone and transcardially perfused with ice-cold PBS. Brain specimens (left and right brain parenchyma from naïve animals; left and right brain parenchyma and tumor tissue from animals with gliomas) were dissected and dissociated into single-cell suspensions using the Brain Tumor Dissociation Kit (Catalog No. 130-095-942, Miltenyi Biotech, Bergisch Gladbach, North Rhine-Westphalia, Germany). Cells were then resuspended in ice-cold FCM buffer containing Hanks' Balanced Saline Solution (HBSS) without calcium and magnesium, 2% FBS, and 10 mM HEPES. Zombie NIR (BioLegend, San Diego, CA, USA) staining was applied to exclude dead cells (20 min at 4°C), followed by a rinse using an ice-cold FCM buffer. Commercially available rat anti-mouse CD16/32 antibody (BioLegend) staining for Fc-blocking (20 min at 4°C) followed by washing in ice-cold FCM buffer was employed to eliminate non-specific binding. The cells were then stained with fluorochrome-conjugated antibodies for 30 min at 4°C in the dark (Table 1) and washed in ice-cold FCM buffer. All data was collected on an instrument in the Shared FACS Facility obtained using NIH S10 Shared Instrument Grant (S10RR027431-01) and analyzed using Flowjo 10 software version 10.6.1 (Tree Star Inc.).

Lymphocytes and myeloid cells were identified from viable cells through the cell membrane markers CD45 and CD11b. Microglia, monocytes and neutrophils were identified from myeloid cells through the expression of CX3CR1-GFP and CCR2-RFP. F4/80 was used to differentiate monocyte-derived tumor-associated macrophages (Mo-TAMs) from naïve monocytes (Mo) and microglia-derived tumor-associated

macrophages (Mg-TAMs) from naïve microglia (Mg). CD80 and CD206 were applied to discriminate the CD80+ pro-inflammatory and CD206+ anti-inflammatory microglia and monocytes (Fig. S1, online only).

Statistical analysis

Continuous variables with a normal distribution are expressed as the mean \pm standard deviation (SD). One-way analysis of variance (ANOVA) followed by Dunnett's *post hoc* test was conducted to compare the cell density of CX3CR1-GFP and CCR2-RFP cells between the individual treatment groups FUSx1, FUSx2 and FUSx3 and the Tumor_NO FUS group from histological analysis. A one-way ANOVA followed by *post hoc* Bonferroni correction was obtained for multigroup comparisons of the cells identified with fluorochrome-conjugated antibodies in FCM analysis. Probability values less than 0.05 were considered to indicate statistical significance. The statistical software SPSS version 22 (IBM, Armonk, NY, USA) was used for the statistical analyses.

Results

Confirmation of BBB opening

On baseline imaging pre-MRgFUS, all 30 tumors exhibited enhancement, with heterogeneous enhancement in 24 tumors and homogeneous enhancement in 6 tumors. All of the animals treated with MRgFUS exhibited enhancement on the post-contrast T1-weighted images of brain parenchyma along the sonicated area, both in the tumor (more pronounced enhancement than at baseline) and outside the tumor, indicating successful opening of the BBB by MRgFUS. Immediately after sonication, there was no edema on T2-weighted images and no evidence of hemorrhage induced by MRgFUS on T2*-weighted gradient echo images. The post-FUS *K*trans values increased significantly ($p = 0.03$) compared with the pre-FUS *K*trans values (Fig. 2B).

MRgFUS increases infiltration of CX3CR1-GFP and CCR2-RFP cells into the tumor area

GL26 glioma tissues were diffusely infiltrated with CX3CR1-GFP and CCR2-RFP cells in all animals that received tumors. In the group that was implanted with tumor cells but not treated with FUS (Tumor_No FUS), single-positive CX3CR1-GFP (Fig. 3A, first row, arrows) and CCR2-RFP (Fig. 3A, first row, arrowheads) cells were scattered in the core region of the tumor, and the fluorescent cells were mainly dual-positive cells (Fig. 3A, first row, triangles). There were more CX3CR1-GFP and CCR2-RFP dual-positive cells (Fig. 3A, second row, triangles) at the tumor edge. Single-positive CX3CR1-GFP (Fig. 3A, third row, arrows) and CCR2-RFP (Fig. 3A, third row, arrowheads) cells and dual-positive cells were seen in the peritumoral area, with single-positive CX3CR1-GFP cells seen more frequently than CCR2-RFP cells. In the animals that underwent three sessions of MRgFUS (Fig. 3B), there was a substantial increase in CCR2-RFP and CX3CR1-GFP cells. The quantification analysis revealed a significant increase in the numbers of green cells and red cells in the animals that underwent two and three sessions of MRgFUS (Fig. 3C).

Table 1
Antibodies used in flowcytometry analysis

Epitope	Conjugate	Clone	Concentration (μ L/test)	Supplier	Laser	Filter
CD45	Brilliant Violet 605	30-F11	1.5	BD Biosciences	405 nm Violet	610/20
CD11b	PerCP/Cy5.5	M1/70	5	BioLegend	488 nm Blue	525/50
F4/80	Brilliant Ultraviolet 395	T45-2342	1	BD Biosciences	355 nm UV	379/29
CD206	APC	C068C2	2.5	BioLegend	640 nm Red	670/30
CD80	Brilliant Ultraviolet 737	16-10A1	2	BD Biosciences	355 nm UV	740/30

UV, ultraviolet.

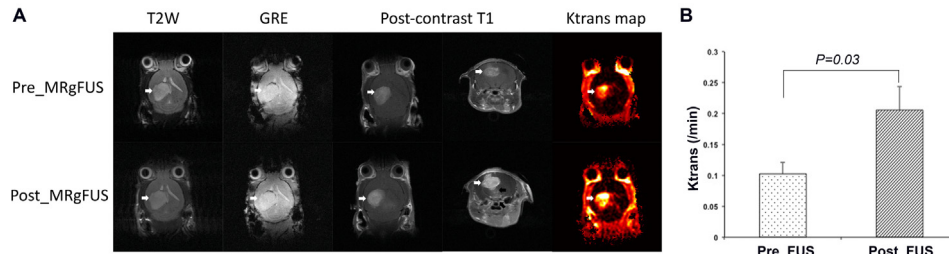


Figure 2. Examples of magnetic resonance images of GL26 allograft acquired before and immediately after magnetic resonance imaging–guided focused ultrasound (MRgFUS). (A) T2-weighted images did not exhibit edema after MRgFUS. The T2*-weighted gradient echo image (GRE) did not exhibit a hemorrhage from MRgFUS. Post-contrast T1-weighted images exhibited enhancement of the tumor both before and after MRgFUS (white arrows), with a more pronounced enhancement on the post-MRgFUS images. Post-contrast T1-weighted images in the axial plane also revealed the enhancement in the brain tissue below the tumor along the path of the ultrasound beam (black arrow). The Ktrans map from the horizontal direction revealed elevated Ktrans in the tumor prior to MRgFUS and an increase in Ktrans signal on MRgFUS induction (white arrows). (B) Pre_FUS versus Post_FUS comparison of Ktrans values for the tumors of the FUSX1 group. The Post_FUS Ktrans values increased significantly from the Pre_FUS values ($p = 0.03$, $n = 5$ in each group).

Immune microenvironment of naïve brain and the brain tissue implanted with GL26 glioma

Microglia (CX3CR1 + CCR2-) constitute the predominant parenchymal immune cell in the naïve brain, the ipsilateral parenchyma and the contralateral parenchyma in the brain allografted with GL26 tumor.

Compared with the naïve brain, the ipsilateral parenchyma of the brains allografted with tumor had more lymphocytes ($p = 0.001$), monocytes ($p = 0.001$) and neutrophils ($p = 0.04$) and relatively lower proportions of microglia ($p = 0.001$). The contralateral parenchyma exhibited the same changes (lymphocytes: $p = 0.001$, monocytes: $p = 0.002$, neutrophils: $p = 0.02$, microglia: $p = 0.002$). The proportions of the immune

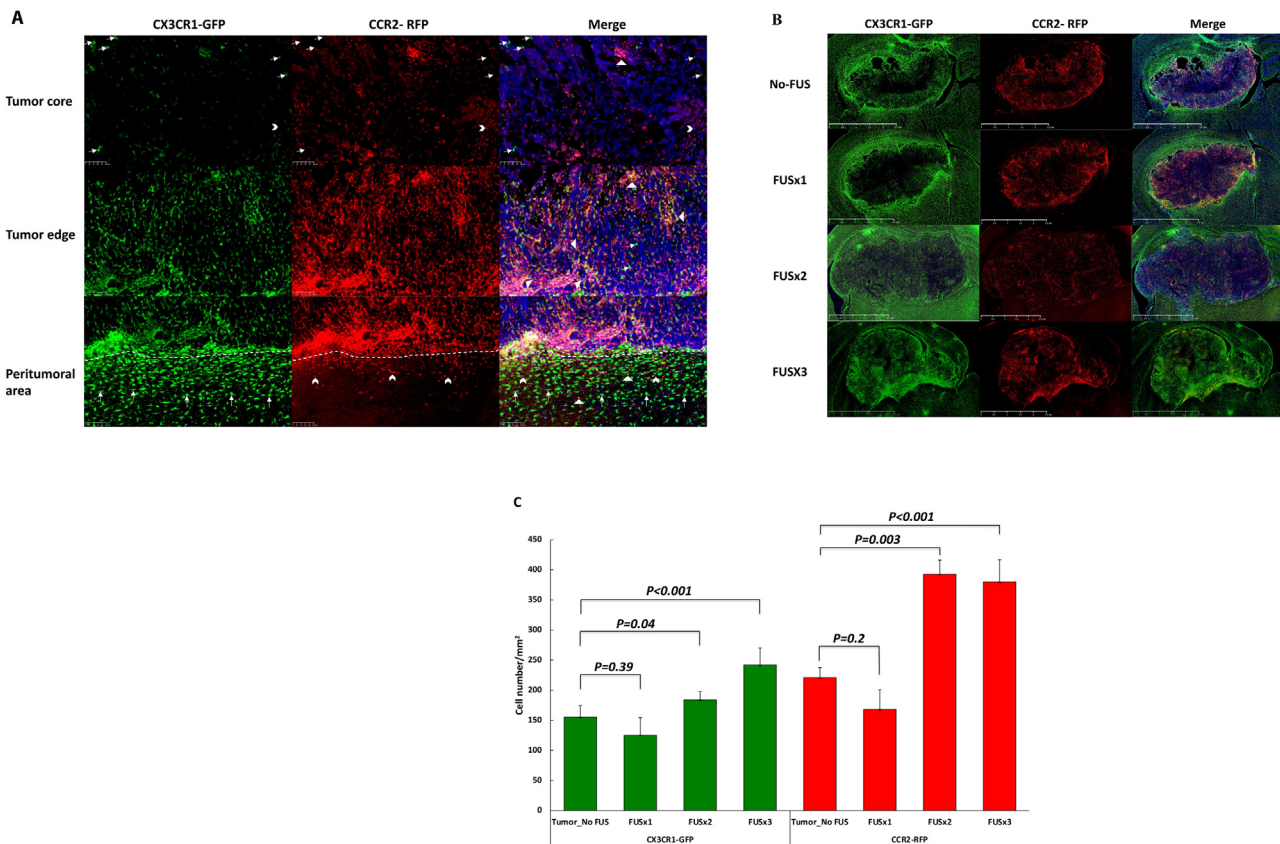


Figure 3. Infiltration of brain tumors by CCR2-RFP and CX3CR1-GFP immune cells. (A) Immunohistochemical staining for CX3CR1-GFP and CCR2-RFP cells for an animal in the tumor-implanted group that did not undergo magnetic resonance imaging–guided focused ultrasound (MRgFUS). The fluorescent immune cells are located mainly at the edges of the tumor and in the peritumoral area, with only a sparse distribution of cells in the core. Both in the tumor core and at the edges, dual-positive cells (first and second rows, triangles) are the predominant type, with occasional single-positive CX3CR1-GFP (first row, arrows) and CCR2-RFP (first and second rows, arrowheads) cells. In the peritumoral area (i.e., the areas below the dotted lines in the lower panels), there are more single-positive CX3CR1-GFP cells than single-positive CCR2-RFP cells, although dual-positive cells are seen in this area as well. (B) Lower-magnification images encompassing the tumor and peritumoral area for four experimental groups. As described in (A), stained cells in the Tumor_No FUS group exhibit stained cells toward the periphery of the tumor and in the peritumoral area. One session of FUS (FUSX1) did not appear to alter the distribution of cells. In contrast, two or three sessions of FUS (FUSX2 and FUSX3, respectively) resulted in increased numbers of immune cells infiltrating the tumor. (C) Quantification of the cell density across the core and periphery of tumors revealed significantly greater infiltration of immune cells into tumors in animals undergoing two or three sessions of FUS.

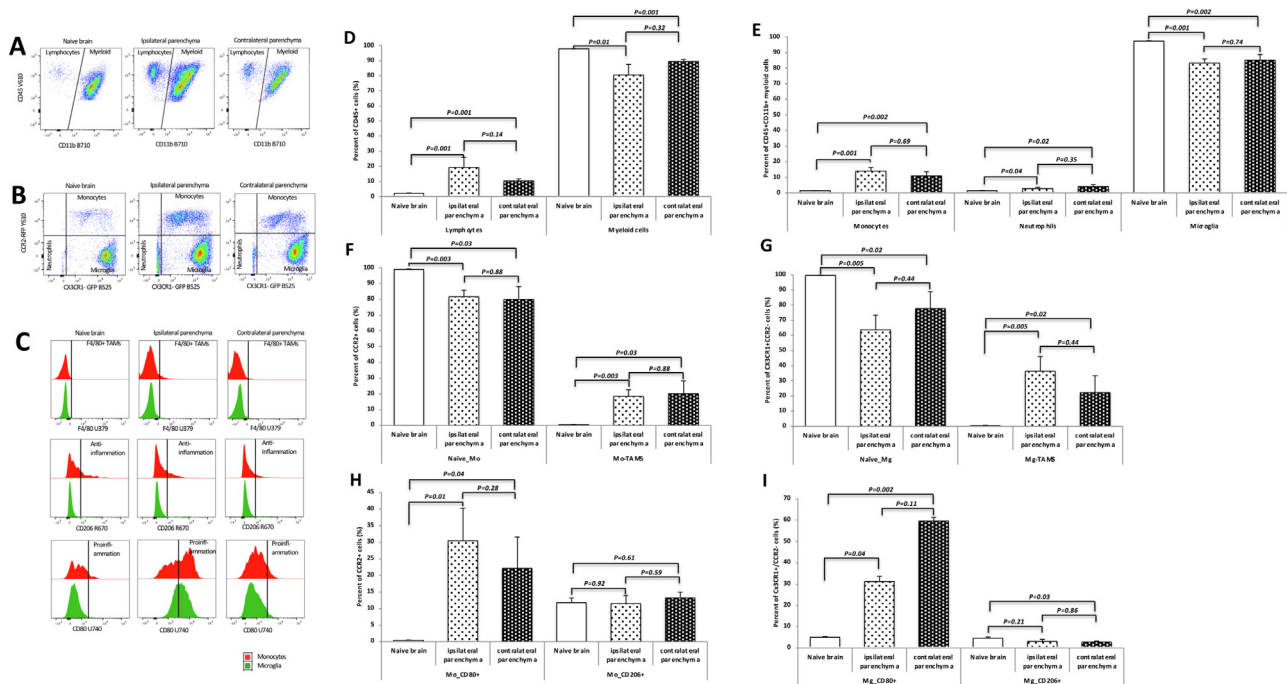


Figure 4. Immune microenvironment of the naïve brain and the brain tissue implanted with GL26 glioma. (A) Dotplots of CD45 + CD11b– lymphocytes and CD45 + CD11b + myeloid cells. Compared with the naïve brain, both ipsilateral and contralateral parenchyma of the brains allografted with tumor exhibited more lymphocytes. (B) Dotplots gated on CX3CR1-GFP and CCR2-RFP from the CD45 + CD11b + myeloid cells. Monocytes were increased in both ipsilateral and contralateral parenchyma. (C) Histogram plots from the staining of F4/80 indicating the differentiation of monocytes and microglia identified from (B); from the staining of CD80 and CD206 indicating the CD80 + pro-inflammation and CD206 + anti-inflammation polarization. (D–I) Quantification of the immune cells identified from (A), (B) and (C). The ipsilateral parenchyma exhibited more lymphocytes ($p = 0.001$) (D), monocytes ($p = 0.001$) (E) and neutrophils ($p = 0.04$) (E) and a relatively lower proportion of microglia ($p = 0.001$) (E). The contralateral parenchyma exhibited the same changes (lymphocytes: $p = 0.001$, monocytes: $p = 0.002$, neutrophils: $p = 0.02$, microglia: $p = 0.002$). The proportions of immune cells between the ipsilateral and contralateral parenchyma did not differ significantly. Compared with naïve brain, the allografted parenchyma exhibited more monocyte-derived TAMs (ipsilateral parenchyma: $p = 0.003$, contralateral parenchyma: $p = 0.03$) (F) and more microglia-derived TAMs (ipsilateral parenchyma: $p = 0.005$, contralateral parenchyma: $p = 0.02$) (G). The bilateral parenchyma of the brain with GL26 glioma did not exhibit significant differences in the differentiation of the monocytes ($p = 0.88$) and microglia ($p = 0.44$) (H, I). There were more pro-inflammatory CD80 + cells in monocytes (ipsilateral parenchyma: $p = 0.01$, contralateral parenchyma: $p = 0.04$) and microglia (ipsilateral parenchyma: $p = 0.04$, contralateral parenchyma: $p = 0.002$) of the ipsilateral and contralateral parenchyma compared with the naïve brain. The proportion of CD206 + cells in the contralateral parenchyma ($p = 0.03$) was lower than that in naïve brain. Mg, microglia; Mo, monocyte; Mg-TAMs, microglia-derived tumor-associated macrophages; Mo-TAMs, monocyte-derived tumor-associated macrophages; naïve-Mg, naïve microglia; naïve-Mo, naïve monocytes.

cells between the ipsilateral and contralateral parenchyma did not differ significantly. Compared with naïve brain, the allografted parenchyma exhibited more monocyte-derived TAMs (ipsilateral parenchyma: $p = 0.003$, contralateral parenchyma: $p = 0.03$), and more microglia-derived TAMs (ipsilateral parenchyma: $p = 0.005$, contralateral parenchyma: $p = 0.02$). The bilateral parenchyma of the brain allografted with tumor did not exhibit significant difference in the differentiation of the monocytes ($p = 0.88$) and microglia ($p = 0.44$).

There were more pro-inflammatory CD80 + cells in monocytes (ipsilateral parenchyma: $p = 0.01$, contralateral parenchyma: $p = 0.04$) and microglia (ipsilateral parenchyma: $p = 0.04$, contralateral parenchyma: $p = 0.002$) of the ipsilateral and contralateral parenchyma compared with the naïve brain. The proportion of CD206 + cells in the contralateral parenchyma ($p = 0.03$) was lower than that in naïve brain (Fig. 4).

Effects of MRgFUS on the immune microenvironment of tumor tissue

The animals treated with MRgFUS exhibited increased monocytes ($p = 0.01$) and decreased proportions of neutrophils ($p = 0.03$) compared with the Tumor_No FUS group. The proportions of lymphocytes ($p = 0.69$), myeloid cells ($p = 0.67$) and microglia ($p = 0.76$) did not significantly differ between the gliomas from the Tumor_No FUS and Tumor_FUS groups (Fig. 5D, 5E). The Tumor_FUS group exhibited more monocyte differentiation, with a higher proportion of monocyte-derived TAMs ($p = 0.04$), whereas microglia did not exhibit changes in

differentiation ($p = 0.19$) (Fig. 5F). In the tumors treated with FUS, there were more pro-inflammatory CD80 + cells both in CCR2 + monocytes ($p = 0.03$) and in CX3CR1 + CCR2– microglia cells ($p = 0.05$) (Fig. 5G, 5H).

Discussion

As the most common and aggressive primary brain tumor, GBMs exhibit a high degree of inter- and intra-tumor heterogeneity. The most prevalent non-neoplastic cell population in the GBM microenvironment comprises cells of the innate immune system called TAMs, which represent approximately 30%–40% of the cells in a GBM [40]. These cells have been reported to engage in reciprocal interactions with neoplastic tumor cells either to inhibit or to promote tumor growth and progression [41,42]. Efforts have been made to achieve a “re-education” of TAMs by polarizing them toward an M1-like pro-inflammatory signature from an M2-like anti-inflammatory/tumorigenic signature, with the goal of creating a less supportive tumor microenvironment [43,44]. The purpose of the present study was to evaluate the possibility that treatment with MRgFUS can modify the immune status of the tumor microenvironment in a model of GBM.

As a non-invasive technique that can induce transient BBB opening in targeted brain regions, MRgFUS combined with microbubbles has been reported to successfully deliver large molecules into the brain parenchyma without evidence of microhemorrhages [45,46]. This approach

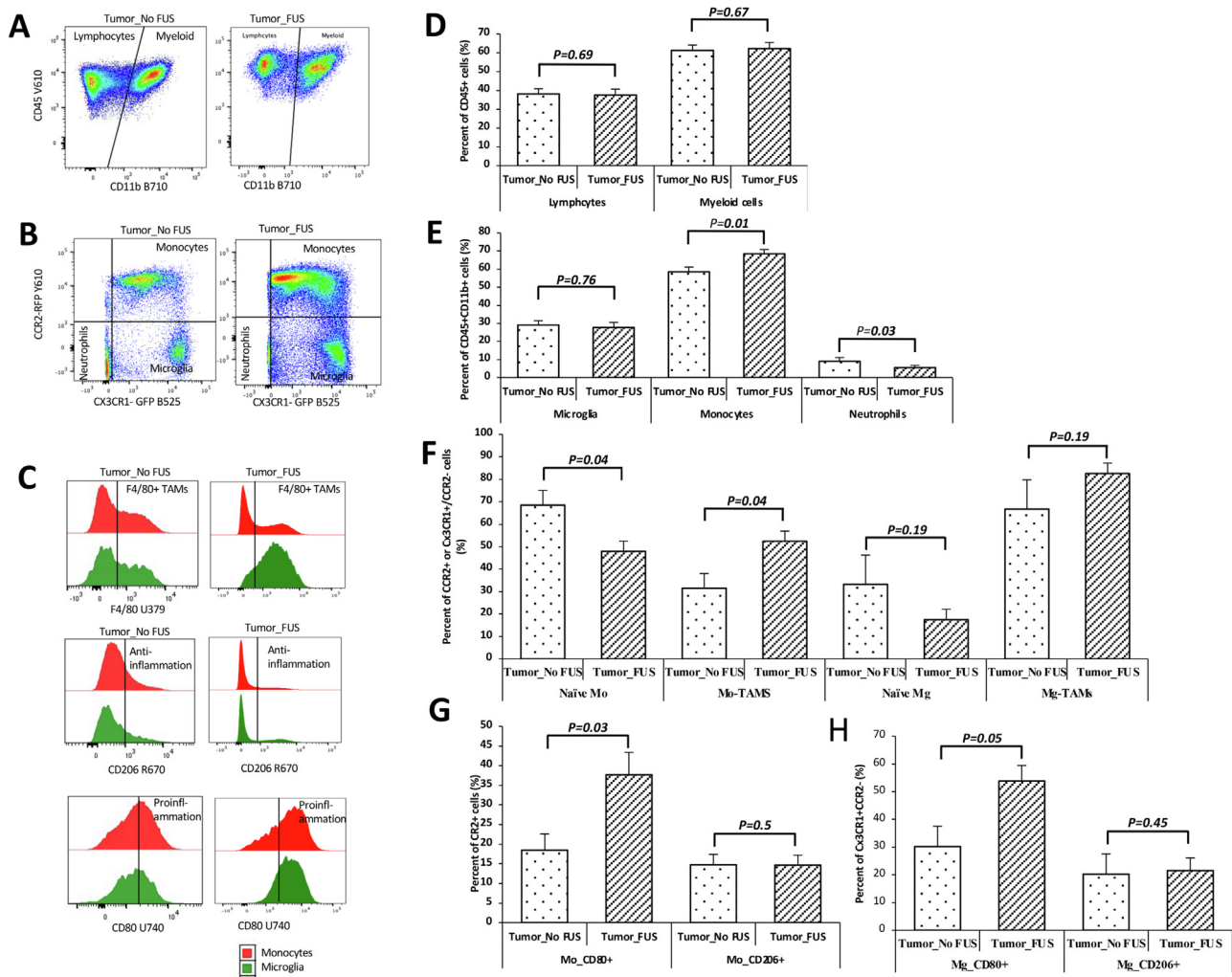


Figure 5. Effects of magnetic resonance imaging–guided focused ultrasound (MRgFUS) on the immune microenvironment of tumor tissue. (A) Dotplots of the CD45 + Cd11b– lymphocytes and CD45 + CD11b + myeloid cells. (B) Dotplots of the cells gated on CX3CR1-GFP and CCR2-RFP from myeloid cells; the tumor treated with FUS exhibited more cells in the monocyte quadrant. (C) Histograms of the monocytes and microglia cells identified through markers of F4/80, CD80 and CD206. (D–H) Quantification of the cell populations identified from (A), (B) and (C). The animals treated with MRgFUS had increased monocytes ($p = 0.01$) and decreased proportions of neutrophils ($p = 0.03$) compared with the Tumor_No FUS group. The proportions of lymphocytes ($p = 0.69$), myeloid cells ($p = 0.67$) and microglia ($p = 0.76$) did not significantly differ between the gliomas from the Tumor_No FUS and Tumor_FUS groups (D and E). The Tumor_FUS group exhibited more monocyte differentiation—a higher proportion of monocyte-derived TAMs ($p = 0.04$)—whereas microglia did not exhibit changes in differentiation ($p = 0.19$) (F). In the tumors treated with FUS, there were more pro-inflammatory CD80 + cells both in CCR2 + monocytes ($p = 0.03$) and in CX3CR1 + CCR2– microglia cells ($p = 0.05$). Mg, microglia; Mo, monocyte; Mg-TAMs, microglia-derived tumor-associated macrophages; Mo-TAMs, monocyte-derived tumor-associated macrophages; naïve-Mg, naïve microglia; naïve-Mo, naïve monocytes.

has been used to facilitate the delivery of drugs and genes to treat stroke, neurodegenerative disease and primary and metastatic brain tumors in animal models [47–50]. Promising findings from extensive animal research led to clinical trials in patients with GBM (NCT02253212, NCT04118764) and Alzheimer disease (AD) (NCT04118764). Initial feasibility and safety were established in patients with GBM [51] and AD [52], with corresponding trials reporting safe and reversible BBB opening using a clinical MR-guided focused ultrasound system.

In addition, MRgFUS by itself may directly exert certain immune-related effects. In studies of normal brain, MRgFUS combined with microbubbles induces microglia activation [23,53,54] and elicits macrophage homing from the periphery to sonicated regions of the brain [23]. Studies using mouse models of AD have reported that repeated MRgFUS treatments lead to a 20% reduction in amyloid- β plaque load [48,55], effects that may be the result of MRgFUS-induced increases in endogenous immunoglobulins, activated microglia and activated astrocytes. Although sterile inflammation, microglial activation and macrophage homing produced by MRgFUS have been well studied, little is known about how MRgFUS affects the cellular phenotypes of TAMs.

In our study, histological assessments did not reveal significant changes in the CX3CR1-GFP or CCR2-RFP cells in tumors that received only one session of MRgFUS. However, tumors that received two or three sessions of MRgFUS exhibited increased numbers of CX3CR1-GFP and CCR2-RFP cells, with the animals receiving three sessions exhibiting the most abundant increases. One limitation of using histological quantification of cellular phenotypes is the difficulty in defining the number of dual-positive cells, which form the predominant population of TAMs. Consequently, to distinguish among the CX3CR1-GFP, CCR2-RFP and CX3CR1-GFP/CCR2-RFP dual positive cells in the TAM pool, FCM was used to analyze the immune cells in naïve brain parenchyma, in brain parenchyma ipsilateral and contralateral to a tumor and in brain tumors that did or did not receive MRgFUS treatment. In naïve brains, almost all of the myeloid cells were CX3CR1 + CCR2– microglia. Implantation of GL26 glioma cells into the brain significantly modified the immune environment of the brain parenchyma. In both the ipsilateral and contralateral parenchyma of the brains implanted with GL26 glioma, the proportions of lymphocytes, monocytes, neutrophils and differentiated cells, including monocyte-derived TAMs and microglia-derived TAMs,

were significantly increased, while the proportion of microglia was decreased. Both monocytes and microglia exhibited more pro-inflammatory CD80+ cells.

The FCM findings revealed an increase in monocytes in tumors treated with MRgFUS, which is consistent with findings from previous studies reporting that MRgFUS causes macrophages to home to a sonicated region [23]. The tumors treated with MRgFUS exhibited more differentiated TAMS from monocytes. These findings indicate that MRgFUS induces homing of monocytes and promotes differentiation of TAMS. Previous studies investigated sterile inflammation from the BBB opening induced by MRgFUS in different species of laboratory animals [23,24], with various microbubble formulations or doses. Kovacs et al. [23] infused 100 μ L Optison into 8- to 10-wk-old Sprague-Dawley rats and sonicated with a single-element spherical FUS transducer with the center frequency at 589.636 KHz. McMahon et al. [24] administered Definity at 20 μ L/kg to Sprague-Dawley rats weighing 200–300 g, and sonicated with a transducer at a frequency of 551.5 kHz. In this study, a transducer at 1.5 MHz was used to sonicate mouse brain with glioma, with Definity microbubbles diluted by 1:20 at 300 μ L/kg body weight, which has been proven to successfully open the mouse BBB in our previous studies.

Under physiological conditions, immune cells in naïve brains do not exhibit pro-inflammatory or anti-inflammatory phenotypes, based on the lack of CD80+ or CD206+ cells. The animals from the Tumor_FUS group had more CD80+ cells in both monocytes and microglia, while the number of CD206+ cells changed. This indicates that MRgFUS induces monocytes and microglia in the direction of pro-inflammatory polarization. This may be the result of the increased expression of cytokines after MRgFUS. Previous evidence of MRgFUS-induced sterile inflammation in normal brain [23] has shown an immediate increase in multiple cytokines including tumor necrosis factor α (TNF α), interleukin (IL) -1α , IL- 1β and IL-18. These changes could in turn induce an increase in chemotactic factors for immune cells (monocyte chemoattractant protein-1 [MCP1], granulocyte colony-stimulating factor [G-CSF], granulocyte–macrophage CSF [GM-CSF], macrophage inflammatory protein-3 α [MIP3 α] and RANTES [regulated upon activation, normal T cell expressed and presumably secreted]), among which IL- 1β and TNF α are pro-inflammatory cytokines.

Conclusions

Treatment of tumors with MRgFUS combined with microbubbles promotes the homing and differentiation of monocytes and induces the polarization of monocytes and microglia in a pro-inflammatory direction. This non-invasive procedure therefore holds promise for future development both as a stand-alone therapeutic strategy and as an adjunct strategy for facilitating the delivery of chemotherapeutic agents for the treatment of GBM.

Conflict of interest

The authors declare no competing interests.

Acknowledgments

This work was supported by National Institutes of Health Grants R01 CA217953-01 and R01 NS102194.

Data availability statement

Raw data remain confidential and will not be shared.

Supplementary materials

Supplementary material associated with this article can be found in the online version at doi:10.1016/j.ultrasmedbio.2022.12.006.

References

- [1] Ostrom QT, Patil N, Cioffi G, Waite K, Kruchko C, Barnholtz-Sloan JS. CBTRUS Statistical Report: primary brain and other central nervous system tumors diagnosed in the United States in 2013–2017. *Neuro Oncol* 2020;22:iv1–96.
- [2] Thakkar JP, Dolecek TA, Horbinski C, Ostrom QT, Lightner DD, Barnholtz-Sloan JS, et al. Epidemiologic and molecular prognostic review of glioblastoma. *Cancer Epidemiol Biomarkers Prev* 2014;23:1985–96.
- [3] Louis DN, Perry A, Wesseling P, Brat DJ, Cree IA, Figarella-Branger D, et al. The 2021 WHO Classification of Tumors of the Central Nervous System: a summary. *Neuro Oncol* 2021;23:1231–51.
- [4] Maxwell R, Jackson CM, Lim M. Clinical trials investigating immune checkpoint blockade in glioblastoma. *Curr Treat Options Oncol* 2017;18:51.
- [5] Sarkaria JN, Hu LS, Parney IF, Pafundi DH, Brinkmann DH, Laack NN, et al. Is the blood–brain barrier really disrupted in all glioblastomas? A critical assessment of existing clinical data. *Neuro Oncol* 2018;20:184–91.
- [6] Zhou W, Chen C, Shi Y, Wu Q, Gimple RC, Fang X, et al. Targeting glioma stem cell-derived pericytes disrupts the blood–tumor barrier and improves chemotherapeutic efficacy. *Cell Stem Cell* 2017;21:591–603 e4.
- [7] Gumerlock MK, Belshe BD, Madsen R, Watts C. Osmotic blood–brain barrier disruption and chemotherapy in the treatment of high grade malignant glioma: patient series and literature review. *J Neurooncol* 1992;12:33–46.
- [8] Rodriguez A, Tatter SB, Debinski W. Neurosurgical techniques for disruption of the blood–brain barrier for glioblastoma treatment. *Pharmaceutics* 2015;7:175–87.
- [9] Duskey JT, Bellelli D, Pederzoli F, Vandelli MA, Forni F, Ruozi B, et al. Current strategies for the delivery of therapeutic proteins and enzymes to treat brain disorders. *Int Rev Neurobiol* 2017;137:1–28.
- [10] Lajoie JM, Shusta EV. Targeting receptor-mediated transport for delivery of biologics across the blood–brain barrier. *Annu Rev Pharmacol Toxicol* 2015;55:613–31.
- [11] Jolesz FA, McDannold NJ. Magnetic resonance-guided focused ultrasound: a new technology for clinical neurosciences. *Neurol Clin* 2014;32:253–69.
- [12] Fry FJ, Ades HW, Fry WJ. Production of reversible changes in the central nervous system by ultrasound. *Science* 1958;127:83–4.
- [13] Fry WJ. Intense ultrasound in investigations of the central nervous system. *Adv Biol Med Phys* 1958;6:281–348.
- [14] Hynynen K, McDannold N, Vykhodtseva N, Jolesz FA. Non-invasive opening of BBB by focused ultrasound. *Acta Neurochir Suppl* 2003;86:555–8.
- [15] Treat LH, McDannold N, Zhang Y, Vykhodtseva N, Hynynen K. Improved anti-tumor effect of liposomal doxorubicin after targeted blood–brain barrier disruption by MRI-guided focused ultrasound in rat glioma. *Ultrasound Med Biol* 2012;38:1716–25.
- [16] Mainprize T, Lipsman N, Huang Y, Meng Y, Bethune A, Ironside S, et al. Blood–brain barrier opening in primary brain tumors with non-invasive MR-guided focused ultrasound: a clinical safety and feasibility study. *Sci Rep* 2019;9:321.
- [17] Kinoshita M, McDannold N, Jolesz FA, Hynynen K. Targeted delivery of antibodies through the blood–brain barrier by MRI-guided focused ultrasound. *Biochem Biophys Res Commun* 2006;340:1085–90.
- [18] Jordao JF, Ayala-Grosso CA, Markham K, Huang Y, Chopra R, McLaurin J, et al. Antibodies targeted to the brain with image-guided focused ultrasound reduces amyloid-beta plaque load in the TgCRND8 mouse model of Alzheimer's disease. *PLoS One* 2010;5:e10549.
- [19] Burgess A, Ayala-Grosso CA, Ganguly M, Jordao JF, Aubert I, Hynynen K. Targeted delivery of neural stem cells to the brain using MRI-guided focused ultrasound to disrupt the blood–brain barrier. *PLoS One* 2011;6:e27877.
- [20] Noroozian Z, Khima K, Huang Y, Kaspar BK, Kugler S, Hynynen K, et al. MRI-guided focused ultrasound for targeted delivery of rAAV to the brain. *Methods Mol Biol* 2019;1950:177–97.
- [21] Aryal M, Arvanitis CD, Alexander PM, McDannold N. Ultrasound-mediated blood–brain barrier disruption for targeted drug delivery in the central nervous system. *Adv Drug Deliv Rev* 2014;72:94–109.
- [22] Arvanitis CD, Askoxylakis V, Guo Y, Datta M, Kloepper J, Ferraro GB, et al. Mechanisms of enhanced drug delivery in brain metastases with focused ultrasound-induced blood–tumor barrier disruption. *Proc Natl Acad Sci USA* 2018;115:E8717–26.
- [23] Kovacs ZI, Kim S, Jikaria N, Qureshi F, Milo B, Lewis BK, et al. Disrupting the blood–brain barrier by focused ultrasound induces sterile inflammation. *Proc Natl Acad Sci USA* 2017;114:E75–84.
- [24] McMahon D, Bendayan R, Hynynen K. Acute effects of focused ultrasound-induced increases in blood–brain barrier permeability on rat microvascular transcriptome. *Sci Rep* 2017;7:45657.
- [25] Chen H, Hou GY, Han Y, Payen T, Palermo CF, Olive KP, et al. Harmonic motion imaging for abdominal tumor detection and high-intensity focused ultrasound ablation monitoring: an in vivo feasibility study in a transgenic mouse model of pancreatic cancer. *IEEE Trans Ultrason Ferroelectr Freq Control* 2015;62:1662–73.
- [26] Chen PY, Hsieh HY, Huang CY, Lin CY, Wei KC, Liu HL. Focused ultrasound-induced blood–brain barrier opening to enhance interleukin-12 delivery for brain tumor immunotherapy: a preclinical feasibility study. *J Transl Med* 2015;13:93.
- [27] Saederup N, Cardona AE, Croft K, Mizutani M, Cotleur AC, Tsou CL, et al. Selective chemokine receptor usage by central nervous system myeloid cells in CCR2-red fluorescent protein knock-in mice. *PLoS One* 2010;5:e13693.
- [28] Jung S, Aliberti J, Graemmel P, Sunshin MJ, Kreutzberg GW, Sher A, et al. Analysis of fractalkine receptor CX(3)CR1 function by targeted deletion and green fluorescent protein reporter gene insertion. *Mol Cell Biol* 2000;20:4106–14.
- [29] Chen Z, Feng X, Herting CJ, Garcia VA, Nie K, Pong WW, et al. Cellular and molecular identity of tumor-associated macrophages in glioblastoma. *Cancer Res* 2017;77:2266–78.

- [30] Zhang Y, Aubry JF, Zhang J, Wang Y, Roy J, Mata JF, et al. Defining the optimal age for focal lesioning in a rat model of transcranial HIFU. *Ultrasound Med Biol* 2015;41:449–55.
- [31] Zhang Y, Tan H, Bertram EH, Aubry JF, Lopes MB, Roy J, et al. Non-invasive, focal disconnection of brain circuitry using magnetic resonance-guided low-intensity focused ultrasound to deliver a neurotoxin. *Ultrasound Med Biol* 2016;42:2261–9.
- [32] Zhang Y, Zhou H, Qu H, Liao C, Jiang H, Huang S, et al. Effects of non-invasive, targeted, neuronal lesions on seizures in a mouse model of temporal lobe epilepsy. *Ultrasound Med Biol* 2020;46:1224–34.
- [33] Anzalone N, Castellano A, Cadioli M, Conte GM, Cuccarini V, Bizzi A, et al. Brain gliomas: multicenter standardized assessment of dynamic contrast-enhanced and dynamic susceptibility contrast MR images. *Radiology* 2018;287:933–43.
- [34] Jirik R, Taxt T, Macicek O, Bartos M, Kratochvila J, Soucek K, et al. Blind deconvolution estimation of an arterial input function for small animal DCE-MRI. *Magn Reson Imaging* 2019;62:46–56.
- [35] Schindelin J, Arganda-Carreras I, Frise E, Kaynig V, Longair M, Pietzsch TA, et al. Fiji: an open-source platform for biological-image analysis. *Nat Methods* 2012;9:676–82.
- [36] Kuwahara M, Eiho S. [Image processing technics—focus on software. 1. Perspectives in biomedical image processing]. *Iyodenshi To Seitai Kogaku* 1983;21:266–73 [in Japanese].
- [37] Sternberg RS. Biomedical image processing. *Computer* 1983;16:22–34.
- [38] Vala HJ, Baxi AB. review on Otsu image segmentation algorithm. *Int J Adv Res Comput Eng Technol* 2013;2:387–9.
- [39] Ankit Chadha NS. A robust approach to image segmentation with optimal thresholding and watershed transform. *Int J Comput Appl* 2013;65:1–7.
- [40] Charles NA, Holland EC, Gilbertson R, Glass R, Kettenmann H. The brain tumor microenvironment. *Glia* 2012;60:502–14.
- [41] Feng X, Szulzewsky F, Yerevanian A, Chen Z, Heinzmann D, Rasmussen RD, et al. Loss of CX3CR1 increases accumulation of inflammatory monocytes and promotes gliomagenesis. *Oncotarget* 2015;6:15077–94.
- [42] Hu F, Dzaye O, Hahn A, Yu Y, Scavetta RJ, Dittmar G, et al. Glioma-derived versican promotes tumor expansion via glioma-associated microglial/macrophages Toll-like receptor 2 signaling. *Neuro-Oncology* 2015;17:200–10.
- [43] Wang Y, Lin YX, Qiao SL, An HW, Ma Y, Qiao ZY, et al. Polymeric nanoparticles promote macrophage reversal from M2 to M1 phenotypes in the tumor microenvironment. *Biomaterials* 2017;112:153–63.
- [44] Chen Z, Hambarzumyan D. Immune microenvironment in glioblastoma subtypes. *Front Immunol* 2018;9:1004.
- [45] Hynynen K, McDannold N, Vykhotseva N, Jolesz FA. Noninvasive MR imaging-guided focal opening of the blood-brain barrier in rabbits. *Radiology* 2001;220:640–6.
- [46] Tung YS, Vlachos F, Choi JJ, Deffieux T, Selert K, Konofagou EE. In vivo transcranial cavitation threshold detection during ultrasound-induced blood–brain barrier opening in mice. *Phys Med Biol* 2010;55:6141–55.
- [47] Burgess A, Dubey S, Yeung S, Hough O, Eterman N, Aubert J, et al. Alzheimer disease in a mouse model: MR imaging-guided focused ultrasound targeted to the hippocampus opens the blood–brain barrier and improves pathologic abnormalities and behavior. *Radiology* 2014;273:736–45.
- [48] Burgess A, Hynynen K. Drug delivery across the blood–brain barrier using focused ultrasound. *Expert Opin Drug Deliv* 2014;11:711–21.
- [49] Kovacs Z, Werner B, Rassi A, Sass JO, Martin-Fiori E, Bernasconi M. Prolonged survival upon ultrasound-enhanced doxorubicin delivery in two syngenic glioblastoma mouse models. *J Control Release* 2014;187:74–82.
- [50] Leinenga G, Langton C, Nisbet R, Gotz J. Ultrasound treatment of neurological diseases—current and emerging applications. *Nat Rev Neurol* 2016;12:161–74.
- [51] Idbaih A, Canney M, Belin L, Desseaux C, Vignot A, Bouchoux G, et al. Safety and feasibility of repeated and transient blood–brain barrier disruption by pulsed ultrasound in patients with recurrent glioblastoma. *Clin Cancer Res* 2019;25:3793–801.
- [52] Lipsman N, Meng Y, Bethune AJ, Huang Y, Lam B, Masellis M, et al. Blood–brain barrier opening in Alzheimer’s disease using MR-guided focused ultrasound. *Nat Commun* 2018;9:2336.
- [53] Alonso A, Reinz E, Fatar M, Hennerici MG, Meairs S. Clearance of albumin following ultrasound-induced blood–brain barrier opening is mediated by glial but not neuronal cells. *Brain Res* 2011;1411:9–16.
- [54] Sinharay S, Tu TW, Kovacs ZI, Schreiber-Stainthorpe W, Sundby M, et al. In vivo imaging of sterile microglial activation in rat brain after disrupting the blood–brain barrier with pulsed focused ultrasound: [¹⁸F]DPA-714 PET study. *J Neuroinflammation* 2019;16:155.
- [55] Jordao JF, Thevenot E, Markham-Coultes K, Scarcelli T, Weng YQ, Xhima K, et al. Amyloid-beta plaque reduction, endogenous antibody delivery and glial activation by brain-targeted, transcranial focused ultrasound. *Exp Neurol* 2013;248:16–29.